GEOPHYSICS, VOL. 69, NO. 1 (JANUARY-FEBRUARY 2004); P. 108–119, 14 FIGS.
10.1190/1.1649380

3D magnetotelluric modeling using the T-Ω finite-element method

Yuji Mitsuhata* and Toshihiro Uchida*

ABSTRACT

We present a finite-element algorithm for computing MT responses for 3D conductivity structures. The governing differential equations in the finite-element method are derived from the **T**–Ω Helmholtz decomposition of the magnetic field **H** in Maxwell's equations, in which **T** is the electric vector potential and Ω is the magnetic scalar potential. The Coulomb gauge condition on **T** necessary to obtain a unique solution for **T** is incorporated into the magnetic flux density conservation equation. This decomposition has two important benefits. First, the only unknown variable in the air is the scalar value of Ω. Second, the curl–curl equation describing **T** is only defined in the earth. By comparison, the system of curl–curl equations for **H** and the electric field **E** are singular in the air, where the conductivity σ is zero. Although the use of a small but nonzero value of σ in the air and application of a divergence correction are usually necessary in the **E** or **H** formulation, the **T**–Ω method avoids this necessity. In the finite-element approximation, **T** and Ω are represented by the edge-element and nodal-element interpolation functions within each brick element, respectively. The validity of this modeling approach is investigated and confirmed by comparing modeling results with those of other numerical techniques for two 3D models.

INTRODUCTION

Three-dimensional EM surveys are becoming increasingly feasible because of recent improvements in 3D modeling techniques. The three commonly used modeling methodologies are the integral equation, finite difference, and finite element. The finite-difference approach, conventionally based on a Taylor series expansion of partial differential equations, is now often based on integral forms of partial differential equations (Mackie et al., 1994). The finite-volume method (e.g., Saad, 1996) has also been used for 3D modeling of EM responses (Haber et al., 2000), and it derives from the conservation law of a flux. Each of these modeling methods has particular advantages: for example, in integral-equation methods, series expansion solutions can be implemented quickly (Zhdanov and Fang, 1996; Avdeev et al., 1997). The use of staggered grids in finite-difference and finite-volume techniques has recently become popular, conserving a magnetic flux and an electric current (Smith, 1996a) and allowing for realistic discontinuous fields. In addition, the convergence of solutions has been greatly accelerated by adopting Krylov subspace methods, various preconditioning techniques, and divergence corrections (Mackie et al., 1994; Smith, 1996b; Sasaki, 1999). Generally, however, finite-element methods are still not widely used in 3D EM modeling of geophysical problems, and few improvements have been published recently. Ellis (1999) uses edge elements to model airborne EM data, and Zyserman and Santos (2000) develop a parallel finite-element algorithm with domain decomposition for MT modeling. Zanoubi et al. (1999) use edge elements and the spectral Lanczos decomposition solver for well-log modeling, and Badea et al. (2001) calculate well-log responses with respect to the Coulomb gauge magnetic vector potential **A** and the electric scalar potential ϕ using nodal elements.

In the finite-difference, finite-volume, and finite-element methods, the governing equations are usually derived directly for the electric field (Newman and Alumbaugh, 1995; Smith, 1996a, b; Sasaki, 1999; Zanoubi et al., 1999) or the magnetic field (Mackie et al., 1994). This approach yields a system of equations that is singular in the air (Haber et al., 2000; Aruliah et al., 2001), requiring the conductivity of air to be approximated by a small, finite value. Consequently, the use of a divergence correction becomes indispensable, especially in the air (Mackie et al., 1994; Sasaki, 1999). The Helmholtz decomposition of the electric field into **A** and ϕ in conjunction with the Coulomb gauge condition $\nabla \cdot \mathbf{A} = 0$ is a popular approach in EM engineering (referred to as the **A**–ϕ method) that has been applied recently in geophysics (LaBrecque, 1999; Haber et al., 2000; Aruliah et al., 2001; Badea et al., 2001). Incorporating the Coulomb gauge condition makes the governing equation elliptic in the air, avoiding the singularity (Haber et al., 2000;

Manuscript received by the Editor March 21, 2002; revised manuscript received July 31, 2003.
*National Institute of Advanced Industrial Science and Technology, Institute for Geo-Resources and Environment, 1-1-1 Higashi, No. 7, Tsukuba, Ibaraki, 305-8567, Japan. E-mail: y.mitsuhata@aist.go.jp; uchida-toshihiro@aist.go.jp.

Aruliah et al., 2001). Another approach, in which the magnetic field is decomposed into the electric vector potential **T** and the magnetic scalar potential Ω, is sometimes adopted for eddy current problems in EM engineering (Carpenter, 1977; Biro and Richter, 1991; Albanese and Rubinacci, 1998). This method involves solving the curl–curl equation for **T** inside the conductive region alone, avoiding problems associated with vanishing conductivity in the air. Additionally, the only unknown component in the air is the magnetic scalar potential Ω: This is an advantage over the **A**–ϕ method, where the three components of **A** as well as the scalar value of ϕ must be determined even in the air. Another approach uses **A**,ϕ–Ψ formulations, in which Ψ is another magnetic scalar potential (Everett and Schultz, 1996). In this approach, the magnetic field is described by only Ψ in the air. The conventional **A**–ϕ method is used within the earth, and the Laplace equation with respect to Ψ is solved in the air. This method can also reduce the number of unknown components.

We present a finite-element algorithm based on the **T**–Ω Helmholtz decomposition for 3D MT modeling. The vector field **T** and scalar field Ω are approximated by edge and nodal elements, respectively; the Coulomb gauge condition $\nabla \cdot \mathbf{T} = 0$ is incorporated directly into one of the governing equations to obtain a unique solution. The asymmetrical system of equations derived in this manner is solved using one of the Krylov subspace methods, the biconjugate gradient-stabilized (Bi-CGSTAB) method van der Vorst, 1992), combined with the incomplete LU decomposition (Saad, 1996). To verify the validity of our modeling method, we compare our calculation results with those obtained using other methods for two 3D models considered as part of the international project on the comparison of modeling methods for electromagnetic induction problems (COMMEMI) by Zhdanov et al. (1997).

BASIC THEORY

T–Ω formulations

At the low frequencies used in MT studies (10^4–10^{-3} Hz), displacement currents are negligible, representing what is referred to as an eddy current problem in EM engineering. Under these circumstances, the EM field is described by the diffusive forms of Maxwell's equations with a time-dependent component $e^{i\omega t}$:

$$\nabla \times \mathbf{E} = -i\omega\mu_0\mathbf{H}, \tag{1}$$

$$\nabla \times \mathbf{H} = \mathbf{J} = \sigma\mathbf{E}, \tag{2}$$

where **E** and **H** are the electric and magnetic fields, respectively; **J** is the electric current density; ω is the angular frequency; σ is the spatially variable electrical conductivity; and the magnetic permeability is that of free space μ_0. We separate **H** into the incident magnetic field $\mathbf{H}_0$ and the resultant magnetic field produced by the electric current induced in the earth $\mathbf{H}_c$, such that $\mathbf{H} = \mathbf{H}_0 + \mathbf{H}_c$. Using this definition, equation (2) can be rewritten as

$$\nabla \times \mathbf{H}_0 = \mathbf{0}, \tag{3}$$

$$\nabla \times \mathbf{H}_c = \mathbf{J} = \sigma\mathbf{E}. \tag{4}$$

Since there is no electric current source in MT modeling problems, $\nabla \cdot \mathbf{J} = 0$ is straightforwardly satisfied. Therefore, **J** can be written in terms of the electric vector potential **T** as

$$\mathbf{J} = \nabla \times \mathbf{T}. \tag{5}$$

In the air region V_a (Figure 1), $\mathbf{J} = 0$. Although **T** can be described with a certain scalar potential such that $\mathbf{T} = \nabla\varphi$, it is more convenient to treat **T** as zero in V_a also (Carpenter, 1977; Steele, 1997). Comparing equations (4) and (5) and using the magnetic scalar potential Ω, we can represent $\mathbf{H}_c$ as

$$\mathbf{H}_c = \mathbf{T} - \nabla\Omega \tag{6}$$

since $\nabla \times (\nabla\Omega) = 0$. Substituting equations (5) and (6) into equation (1), we obtain the following curl–curl equation for the interior of the earth (V_c) as the first equation:

$$\nabla \times \left(\frac{1}{\sigma}\nabla \times \mathbf{T}\right) + i\omega\mu_0(\mathbf{T} - \nabla\Omega) = -i\omega\mu_0\mathbf{H}_0 \quad \text{in} \quad V_c. \tag{7}$$

As the second equation, the scalar equation is obtained by combining the conservative law for the magnetic flux density $\mathbf{B}_c = \mu_0\mathbf{H}_c$,

$$\nabla \cdot \mathbf{B}_c = 0, \tag{8}$$

with equation (6), giving

$$\nabla \cdot (\mathbf{T} - \nabla\Omega) = 0 \quad \text{in} \quad V \tag{9}$$

because μ_0 is constant in the whole region. This is satisfied throughout the whole problem domain $V (= V_a \cup V_c \cup S_c)$ with $\mathbf{T} = 0$ in V_a.

Equations (7) and (9) can be used to determine **T** and Ω, an approach referred to as the **T**–Ω method (e.g., Tsuboi and Naitoh, 1994; Steele, 1997). In some studies, **T** and Ω are referred to as the current density vector potential (Albanese and Rubinacci, 1998) and the reduced magnetic scalar potential (Silvester and Ferrari, 1996), respectively. However, equations (7) and (9) cannot be uniquely solved because they are not independent of each other: the divergence of equation (7) leads to equation (9) because the divergence of the first term on the left-hand side of equation (7) and $\nabla \cdot (\mu_0\mathbf{H}_c)$ both equal

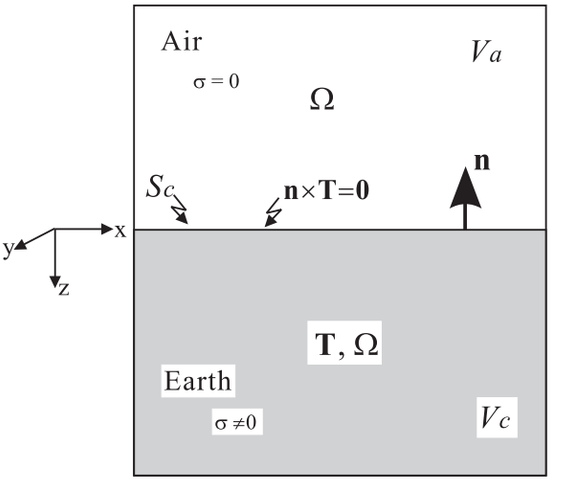

FIG. 1. Schematic of the MT forward problem. The air, earth, and earth's surface are denoted by V_a, V_c, and S_c, respectively; **n** is the outward unit normal vector to S_c.

zero. To overcome this nonuniqueness, we adopt the Coulomb gauge:

$$\nabla \cdot \mathbf{T} = 0 \quad \text{in} \quad V_c. \tag{10}$$

In the finite-element method using nodal elements, equation (10) is incorporated into equation (7) as a penalty (e.g., Biro and Richter, 1991). In recent approaches using edge elements in EM engineering, however, the gauge condition based on the tree–cotree decomposition is used (Albanese and Rubinacci, 1998). In our study, we substitute equation (10) into equation (9) and reformulate equation (9), as shown later. In particular, the Coulomb gauge condition is incorporated when deriving the governing differential equations.

Interface conditions

We next consider the conditions imposed on $\mathbf{T}$ and Ω at the interface between two media, medium 1 and medium 2, with different values of conductivity. At the interface, the tangential component of $\mathbf{H}$ is continuous (e.g., Harrington, 1961) and therefore

$$\mathbf{n} \times (\mathbf{H}_1 - \mathbf{H}_2) = \mathbf{0}, \tag{11}$$

where $\mathbf{n}$ is the unit vector normal to the interface. This condition can be split into two by defining interface conditions in terms of the tangential component of $\mathbf{T}$ and the value of Ω (Biro and Richter, 1991):

$$\mathbf{n} \times (\mathbf{T}_1 - \mathbf{T}_2) = \mathbf{0} \tag{12}$$

and

$$\Omega_1 = \Omega_2. \tag{13}$$

At the air–earth interface S_c, $\mathbf{J}$ cannot flow out into the air and we must impose

$$\mathbf{n} \cdot \mathbf{J} = 0 \quad \text{at} \quad S_c, \tag{14}$$

where $\mathbf{n}$ is the unit normal vector from the earth toward the air. Integrating equation (14) at S_c and substituting equation (5), we obtain, via Stokes' theorem,

$$\int_{S_0} \mathbf{n} \cdot \mathbf{J} dS = \int_{S_0} \mathbf{n} \cdot (\nabla \times \mathbf{T}) dS = \oint_{C_0} \mathbf{T} \cdot \mathbf{t} dl = 0, \tag{15}$$

where S_0 is a certain area in S_c, C_0 is a closed curve bounding S_0, and $\mathbf{t}$ is the unit vector tangential to C_0. Bearing in mind that equation (15) is satisfied for any arbitrary C_0 in S_c, we can write equation (15) as $\mathbf{T} \cdot \mathbf{t} = 0$ at S_c. Since $\mathbf{t}$ lies within the surface S_c, $\mathbf{T} \cdot \mathbf{t} = 0$ is equivalent to

$$\mathbf{n} \times \mathbf{T} = \mathbf{0} \quad \text{at} \quad S_c, \tag{16}$$

which can be imposed as an interface condition at S_c (Miya, 1995).

There is another important consideration to make regarding S_c. At any interface within V_c, the Coulomb gauge condition [equation (10)] requires continuity of the normal component of $\mathbf{T}$. Equation (16) implies that a normal component of $\mathbf{T}$ exists at S_c; but, as shown, $\mathbf{T}$ is zero in V_a. Clearly, the normal component of $\mathbf{T}$ is discontinuous across S_c. The Coulomb gauge condition cannot be satisfied there, and then it cannot be imposed in equation (9) because equation (9) should be satisfied in V including S_c. In Appendix A we present the derivation of a more general divergence condition (that incorporates the Coulomb gauge condition), in which topography described by $g(x, y) = z$ is treated. As a result, we obtain

$$\nabla \cdot \mathbf{T}(\mathbf{r}) = -\mathbf{n} \cdot \mathbf{T}(\mathbf{r}) |\nabla f| \delta(\mathbf{r} \in S_c) \quad \text{in} \quad V \tag{17}$$

instead of equation (10), where δ is the Dirac delta function and $f = z - g(x, y)$. Equation (17) includes the Coulomb gauge condition in V_c. Substituting equation (17) into equation (9), we finally obtain

$$\nabla^2 \Omega(\mathbf{r}) = -\mathbf{n} \cdot \mathbf{T}(\mathbf{r}) |\nabla f| \delta(\mathbf{r} \in S_c) \quad \text{in} \quad V, \tag{18}$$

implying that the source of Ω is the normal component of $\mathbf{T}$ at S_c. In this study, we solve equations (7) and (18) to obtain $\mathbf{T}$ and Ω. We reemphasize that equation (7) is satisfied only in the earth, since $\mathbf{T}$ is fixed at zero in the air. This $\mathbf{T}$–Ω approach uses significantly less computer memory than the conventional $\mathbf{A}$–ϕ method because the only unknown variable in the air is the scalar component Ω. Moreover, Mackie et al. (1994) and Sasaki (1999) show that when iteratively solving the curl–curl equation for $\mathbf{H}$ or $\mathbf{E}$ using staggered-grid, finite-difference (FD) methods, the divergence correction to $\mathbf{H}$ or $\mathbf{E}$ is particularly necessary in the air. It is their representation of the air with a small nonzero conductivity that makes the system of equations ill conditioned. With the $\mathbf{T}$–Ω method, in contrast, such an approximation is unnecessary.

Boundary conditions

To determine the EM fields uniquely, we must specify the tangential components of $\mathbf{H}$ or $\mathbf{E}$ on the boundaries of the computation region V (Harrington, 1961). Similar to the interface conditions, the boundary conditions on the tangential components of $\mathbf{H}$ can be split into two by specifying both the tangential component of $\mathbf{T}$ and the value of Ω. In MT problems, for which the incident magnetic field $\mathbf{H}_0$ has only horizontal components, the vertical component of $\mathbf{T}$ is produced exclusively by 2D or 3D conductivity anomalies. Accordingly, we can see from equation (18) that Ω is generated by the same conductivity anomalies. Assuming the boundaries lie sufficiently far from these anomalies, we apply the Dirichlet condition $\Omega = 0$ at the boundary of V and the condition $T_z = 0$ at the side boundaries of V_c. For a uniform incidence field H_{0x} parallel to x, we impose $T_x = T_{0x}$ at the x–z boundary surfaces of V_c and $T_y = 0$ at the y–z surfaces of V_c , whereT_{0x} is the solution corresponding to an earth model without any 2D or 3D conductivity anomalies. Assuming that the bottom of V_c is sufficiently deeper than the skin depth, we can adopt $T_x = -H_{0x}$ because $H_x = H_{0x} + T_x = 0$ at the bottom. Similar boundary conditions are imposed in the case of a uniform y-directional incident field H_{0y}.

Homogeneous earth response

To illustrate the $\mathbf{T}$–Ω method, we now solve equations (7) and (18) for a homogeneous earth. For a uniform incidence field H_{0x}, the induced field $\mathbf{H}_c$ has only an x-component. Thus,

T also has only an x-component T_x, the right-hand side of equation (18) equals zero, and equation (18) is the Laplace equation. Given the Dirichlet boundary condition $\Omega = 0$ at the boundary of V, the harmonic function satisfying the Laplace equation requires that $\Omega = 0$ throughout V. Since T_x is a function of z only, equation (7) becomes

$$-\frac{1}{\sigma}\frac{\partial^2 T_x}{\partial z^2} + i\omega\mu_0 T_x = -i\omega\mu_0 H_{0x}. \tag{19}$$

For the particular boundary conditions used, namely, $T_x = 0$ at $z = 0$ and $T_x \to -H_{0x}$ as $z \to \infty$, a characteristic solution to this equation is

$$T_x = H_{0x}(e^{-ikz} - 1), \tag{20}$$

where k is the wavenumber given by $k = (-i\omega\mu_0\sigma)^{1/2}$.

FINITE-ELEMENT METHOD ANALYSIS

Edge and nodal elements

We divide the problem domain into a number of bricks and adopt edge and nodal elements (e.g., Jin, 1993) to approximate the **T** and Ω fields, respectively (Figure 2). Each side of a brick is assigned a constant tangential field component of **T**, and each node is assigned a constant value of Ω. Within each brick, σ is assumed to be constant. Representing **T** and Ω within the eth element as $\mathbf{T}^e$ and Ω^e, we can write

$$\mathbf{T}^e = \sum_{i=0}^{11} \mathbf{N}_i^e T_i^e, \tag{21}$$

and

$$\Omega^e = \sum_{j=0}^{7} N_j^e \Omega_j^e, \tag{22}$$

where N_j^e denotes the eight scalar interpolation functions and $\mathbf{N}_i^e$ denotes the 12 vector interpolation functions, given by

$$\mathbf{N}^e_{i\in[0,3]} = N^e_{xi}\hat{\mathbf{x}}, \quad \mathbf{N}^e_{i\in[4,7]} = N^e_{yi}\hat{\mathbf{y}}, \quad \mathbf{N}^e_{i\in[8,11]} = N^e_{zi}\hat{\mathbf{z}}, \tag{23}$$

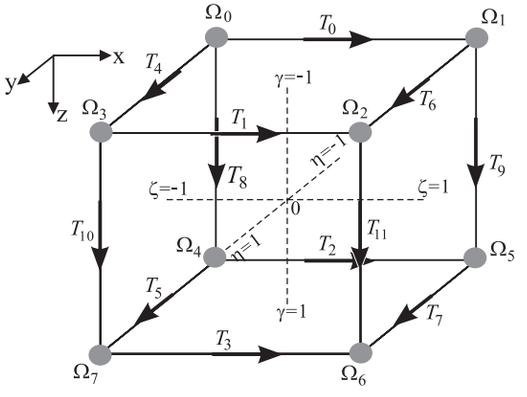

FIG. 2. Sampling points for **T** and Ω in the brick element and the local coordinate system. In each brick, the vector field **T** is approximated by the twelve components assigned at the centers of edges; the scalar field Ω is approximated by the eight components at the vertices. Within each brick, σ is assumed to be constant.

with respect to unit vectors $\hat{\mathbf{x}}$, $\hat{\mathbf{y}}$, and $\hat{\mathbf{z}}$ parallel to the x, y, and z axes, respectively. As a matter of convenience, we use a local coordinate system (ξ, η, γ) within each element, as shown in Figure 2. The local coordinates are given by $\xi = 2(x - x_c^e)/l_x^e$, $\eta = 2(y - y_c^e)/l_y^e$, and $\gamma = 2(z - z_c^e)/l_z^e$, where x_c^e, y_c^e, and z_c^e denote the coordinate of the center of the eth element and where l_x^e, l_y^e, and l_z^e denote the side lengths of the eth element in the x-, y-, and z-directions, respectively. We can then express N_j^e as

$$N^e_{j\in[0,7]} = \frac{1}{8}(1 + \xi\xi_j)(1 + \eta\eta_j)(1 + \gamma\gamma_j). \tag{24}$$

The values N_{xi}^e, N_{yi}^e, and N_{zi}^e in equation (23) are expressed by

$$N_{xi}^e = \frac{1}{4}(1 + \eta\eta_i)(1 + \gamma\gamma_i), \tag{25}$$

$$N_{yi}^e = \frac{1}{4}(1 + \gamma\gamma_i)(1 + \xi\xi_i), \tag{26}$$

and

$$N_{zi}^e = \frac{1}{4}(1 + \xi\xi_i)(1 + \eta\eta_i), \tag{27}$$

where $(\xi_j, \eta_j, \gamma_j)$ is the position of the jth node and $(\xi_i, \eta_i, \gamma_i)$ is the position of the midpoint of the ith edge.

The combined use of edge and nodal elements such as this has been used in some applications of the $\mathbf{A}$–ϕ method to eddy current problems (e.g., Kameari, 1988; Fujiwara et al., 1996). Since Ω is composed of the values assigned at the nodes, the interface condition of equation (13) is automatically satisfied. Moreover, the vector interpolation function also guarantees the continuity of the tangential field of **T**. Since $\mathbf{N}_i^e$ has a tangential component only along the ith edge, the interface condition of equation (12) is automatically satisfied by the expansion given in equation (21) (Jin, 1993).

Galerkin finite-element method

From the governing differential equations (7) and (18), we derive the corresponding system of finite-element method equations using the Galerkin method (e.g., Jin, 1993). We define a residual vector **r** for equation (7) and a scalar residual r for equation (18):

$$\mathbf{r} = \nabla \times \left(\frac{1}{\sigma}\nabla \times \mathbf{T}\right) + i\omega\mu_0(\mathbf{T} - \nabla\Omega) + i\omega\mu_0\mathbf{H}_0, \tag{28}$$

$$r = -\nabla^2\Omega(\mathbf{r}) - \mathbf{n}\cdot\mathbf{T}(\mathbf{r})|\nabla f|\delta(\mathbf{r} \in S_c). \tag{29}$$

The Galerkin method enforces the conditions

$$R_{Tk} = \int_{V_c} \mathbf{N}_k \cdot \mathbf{r} dV = \sum_{e=1}^{NE} \int_{V_c^e} \mathbf{N}^e_{i(k)} \cdot \mathbf{r} dV = 0 \tag{30}$$

and

$$R_{\Omega l} = \int_V N_l r dV = \sum_{e=1}^{NT} \int_{V^e} N^e_{j(l)} r dV = 0, \tag{31}$$

where R_{Tk} is the integral of **r** weighted by $\mathbf{N}_k$ assigned to the kth edge over the entire earth (V_c), $R_{\Omega l}$ is the integral of r weighted by N_l assigned to the lth node over the whole region (V), NE is the number of brick elements in V_c, NT is the total number of brick elements in V, and $i(k)$ and $j(l)$ represent the

local numbers of edges and nodes corresponding to the global numbers k and l in the eth element, respectively.

Calculating the integrals in equations (30) and (31) for each element as shown in Appendix B, we obtain the following matrix expression:

$$\{R^e\} = \begin{bmatrix} \{R^e_\Omega\} \\ \{R^e_T\} \end{bmatrix} = \begin{bmatrix} [G^e] & [Q^e] \\ -i\omega\mu_0[H^e] & \rho^e[E^e] + i\omega\mu_0[F^e] \end{bmatrix} \times \begin{bmatrix} \{\Omega^e\} \\ \{T^e\} \end{bmatrix} + \begin{bmatrix} \{0\} \\ i\omega\mu_0\{P^e\} \end{bmatrix}, \quad (32)$$

where { } and [ ] represent a column vector and a matrix, respectively. The elements of $\{R^e_\Omega\}$ and $\{R^e_T\}$ are the integrals of equations (30) and (31) for eight nodes and 12 edges over the eth element, respectively; $\{\Omega^e\} = \{\Omega^e_0, \ldots, \Omega^e_7\}^T$ and $\{T^e\} = \{T^e_0, \ldots, T^e_{11}\}^T$; $[G^e]$, $[Q^e]$, $[H^e]$, $[E^e]$, and $[F^e]$ are 8×8, 8×12, 12×8, 12×12, and 12×12 matrices, respectively; and $\{P^e\}$ is the source term from the incident magnetic field $\mathbf{H}_0$. Details of the derivations of these submatrices and column vectors are provided in Appendix B. Assembling $\{R^e\}$ over all elements and setting it equal to zero subject to the boundary conditions, we finally obtain the system of equations

$$[A]\{X\} = \{B\}, \quad (33)$$

where $[A]$ is an asymmetrical sparse complex matrix often referred to as the system matrix, $\{X\}$ consists of the unknowns $\{\Omega^e\}$ and $\{T^e\}$, and $\{B\}$ is composed of the last term of equation (32) and the Dirichlet boundary condition.

Solving the finite-element method matrix equation

Equation (33) is a large, sparse, asymmetrical matrix equation of the sort typically solved using Krylov subspace solvers incorporating preconditioning (Barrett et al., 1994). Haber et al. (2000) and Aruliah et al. (2001) use the Bi-CGSTAB method (van der Vorst, 1992) and the incomplete LU (ILU) threshold decomposition for preconditioning to solve similarly large, sparse, asymmetrical matrix equations derived in a finite-volume discretization of the $\mathbf{A}$–ϕ equations. We also use the Bi-CGSTAB method and the incomplete (LU) preconditioner with no fill-in allowed (Saad, 1996).

The Bi-CGSTAB method uses two residual vectors, $\{s\}$ and $\{r\}$, at each iteration, defined by $\{s\} = \{r\} = \{B\} - [A]\{X\}$ (Barrett et al., 1994). When either of the convergence criteria, $\|\{s\}\|^2/\|\{B\}\|^2 \le \varepsilon$ or $\|\{r\}\|^2/\|\{B\}\|^2 \le \varepsilon$, is satisfied given a specified tolerance ε, the iterative process ends. In the examples shown below, $\varepsilon = 10^{-8}$. As demonstrated in the two computation results shown later, computation for solving the finite-element method matrix equation takes much longer than the staggered-grid, finite-difference method (e.g., Sasaki, 1999), apparently because of the larger bandwidth (51 nonzero elements) in matrix $[A]$ compared to that (13 nonzero elements) in the staggered-grid FD method.

RESULTS

We computed MT responses for two different COMMEMI project models (Zhdanov et al., 1997) and compared them with those obtained using other modeling methods. In the following examples, we show apparent resistivity and phase data for the XY and YX modes along profiles across the 3D bodies. An XY mode means the E_x field is generated by the incident H_{oy} field and the apparent resistivity and phase data are calculated from the tentative impedance $Z^*_{xy} = E_x/H_y$. Likewise, YX mode means the E_y field is generated by the incident H_{0x} field, and apparent resistivity and phase data are calculated from the tentative impedance $Z^*_{yx} = -E_y/H_x$. Note that Z^*_{xy} and Z^*_{yx} can be different from the exact off-diagonal components of the impedance tensor, Z_{xy} and Z_{yx}, which can be evaluated straightforwardly from field data generated by two different polarization sources (e.g., Ting and Hohmann, 1981). All computations in the following examples were implemented on a 1-GHz Pentium III PC.

Example 1: COMMEMI 3D-1 model

The first model we consider (model 1) is the COMMEMI 3D-1 model (Figure 3) of an embedded conductive block (0.5 ohm-m) exhibiting a relatively high-conductivity contrast with a homogeneous background earth (100 ohm-m). As the

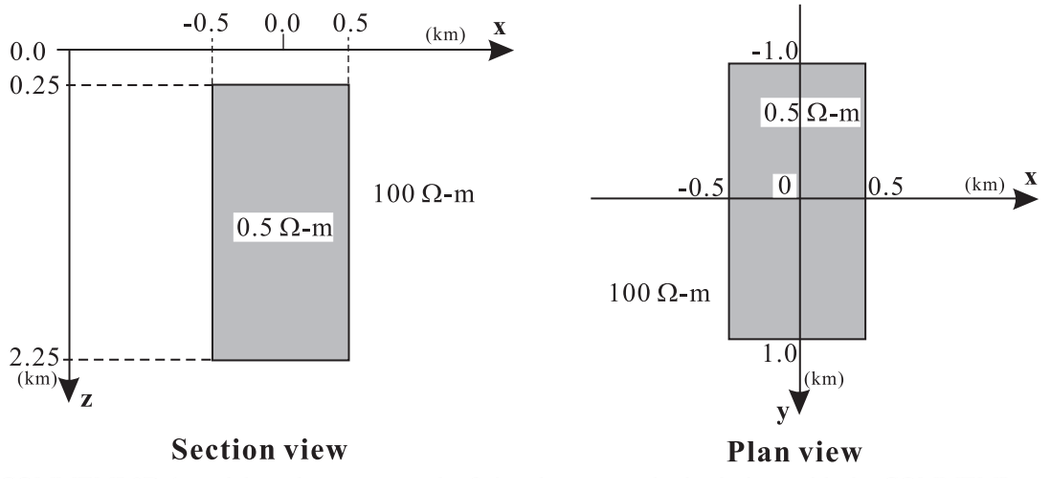

FIG. 3. The COMMEMI 3D-1 model used to compare the finite-element method solutions with the COMMEMI results and the staggered-grid FD solutions. Three-dimensional MT responses were computed at profiles along the x- and y-axes.

boundary condition in our computation, we use the analytical solution of **T** for the 100-ohm-m homogeneous earth represented by equation (20). The COMMEMI project lists 3D modeling results obtained using various modeling methods and the mean values and standard deviations of the apparent resistivity for frequencies of 0.1 and 10 Hz. We also make comparisons with solutions obtained using the staggered-grid finite-difference method for the **E** field (Sasaki, 1999, 2001).

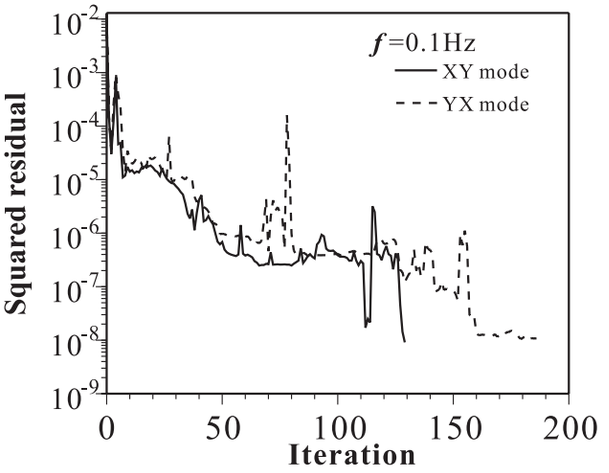

FIG. 4. Plots of the squared residual as a function of iteration number in the Bi-CGSTAB method applied to estimates of the *XY*- and *YX*-mode MT responses for the COMMEMI 3D-1 model at 0.1 Hz. The squared residual is defined as $\|\{B\}-[A]\{X\}\|^2/\|\{B\}\|^2$ [see equation (33)].

To compute the 3D response at 0.1 Hz, we use an irregular mesh with a three-decade difference in grid spacing and a mesh consisting of $24 \times 28 \times 28$ elements to represent a total computational domain of $70 \times 70 \times 140$ km. Figure 4 shows a plot of the squared residual $\|\{r\}\|^2/\|\{B\}\|^2$ versus the iteration number in the Bi-CGSTAB. The squared residuals for the *XY* and *YX* modes exhibit some rising spikes but nevertheless converge after 129 and 186 iterations, respectively. The CPU time for the computations is 688 s for the *XY* mode and 857 s for the *YX* mode. Figures 5 and 6 compare our results with the COMMEMI and staggered-grid FD solutions. With the exception of some discrepancies near the edges of the conductor, our solutions agree very well with the others.

Next, we computed the 3D responses for 10 Hz with a $40 \times 42 \times 28$ irregular mesh. The whole computational domain was $10 \times 10 \times 15$ km. Figure 7 shows the convergence of the *XY* and *YX* modes, which converge after 201 iterations (2454 s of CPU time) and 124 iterations (1665 s), respectively. Figures 8 and 9 compare our results with those from the COMMEMI and staggered-grid FD solutions. The agreement between our solutions and the staggered-grid FD solution is excellent, with the largest discrepancy ($x = 950$ m, Figure 9c) less than 5%. The consistency with the COMMEMI results is generally good, also. However, the *XY*-mode apparent resistivities of the COMMEMI results are larger than those of our solutions and the staggered-grid FD solutions above the

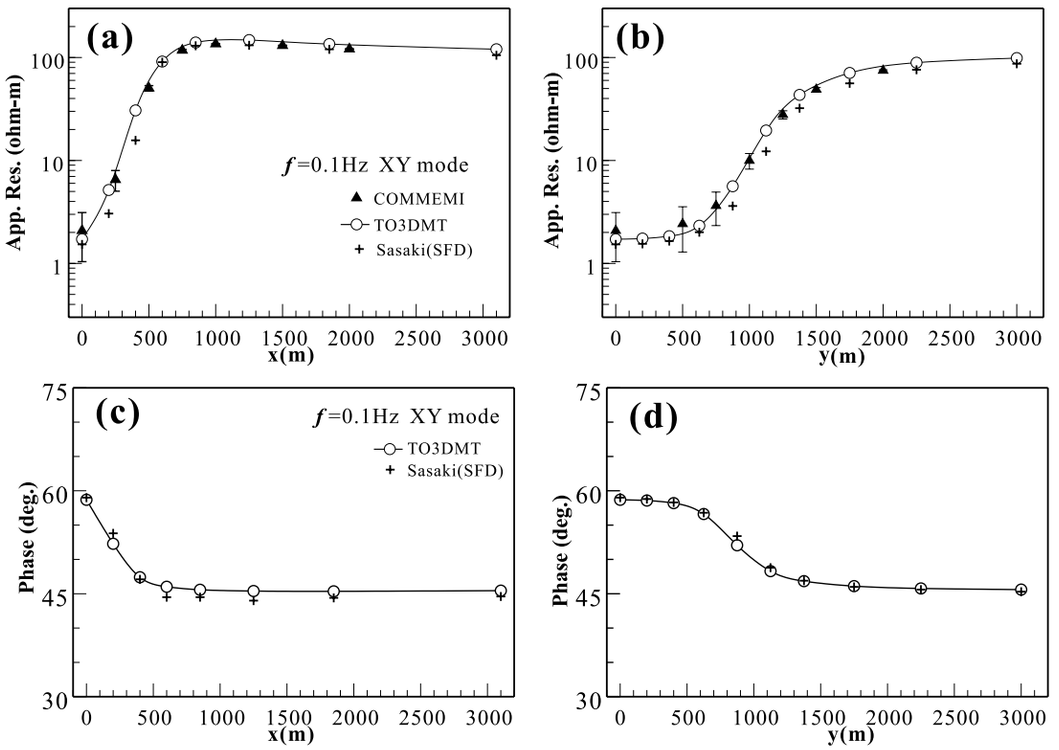

FIG. 5. Comparisons between results obtained using the **T**–Ω FEM (this study; denoted TO3DMT), staggered-grid FD, and COMMEMI results. The *XY*-mode MT response at 0.1 Hz is shown in terms of apparent resistivity along the (a) *x*-axis and (b) *y*-axis; phase data are along the (c) *x*-axis and (d) *y*-axis. The mean apparent resistivities of the COMMEMI results are shown with their standard deviations. No information on the mean values of the phase data was provided in the COMMEMI results.

conductive block ($x < 500$ m and $y < 1000$ m) in Figures 8a and 8b. A similar discrepancy with the COMMEMI results is recognized by Zyserman and Santos (2000), whose results are consistent with ours. The COMMEMI results are the mean values of seven results obtained with integral-equation and finite-difference modeling code, which have large standard errors over the conductive block.

Example 2: COMMEMI 3D-2 model

Model 2 is the COMMEMI 3D-2 model (Figure 10), with which several new modeling methods have been tested (Mackie et al., 1993; Avdeev et al., 1997; Sasaki, 1999; Zyserman and Santos, 2000; Fomenko and Mogi, 2002). This model is comprised of two rectangular blocks embedded adjacent to one another in a three-horizontal-layer structure. The *XY* and *YX* mode responses at 0.001 Hz were computed with a $25 \times 22 \times 21$ irregular mesh, representing an entire computational domain of $400 \times 400 \times 540$ km. The analytical solution for **T** in a three-layered earth was the boundary condition. The Bi-CGSTAB process converged after 396 iterations for the *XY* mode and 368 iterations for the *YX* mode, requiring 1067 and 982 s CPU time, respectively. Figure 11 compares the results obtained using the **T**–Ω method and the integral-equation solutions obtained by Wannamaker (1991), taken from Mackie et al. (1993). The consistency between them is excellent.

CONCLUSIONS

We have developed a finite-element algorithm based on the **T**–Ω decomposition for 3D MT modeling. The Coulomb gauge condition on the electric vector potential **T** is incorporated in the conservation law for magnetic flux density at the level of the governing equations. Both **T** and Ω are represented using the edge-element and nodal-element interpolation functions, respectively, in each brick-shaped finite element. We solve the system of finite-element modeling equations using the Bi-CGSTAB method with the no fill-in incomplete LU decomposition preconditioner. In popular MT modeling schemes

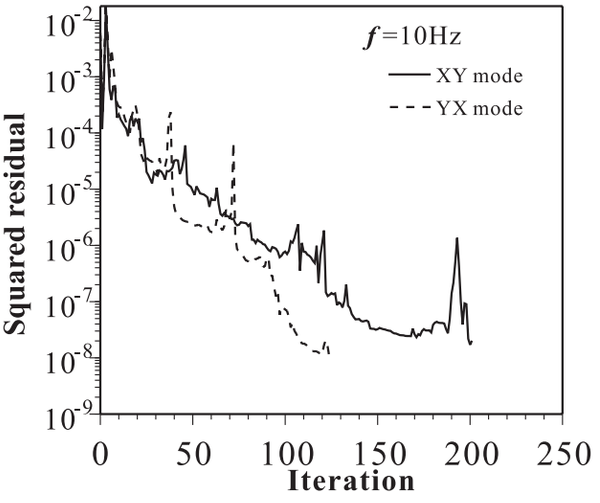

FIG. 7. Plots of the squared residual versus iteration number in the Bi-CGSTAB solution of the *XY*- and *YX*-mode MT responses for the COMMEMI 3D-1 model at 10 Hz.

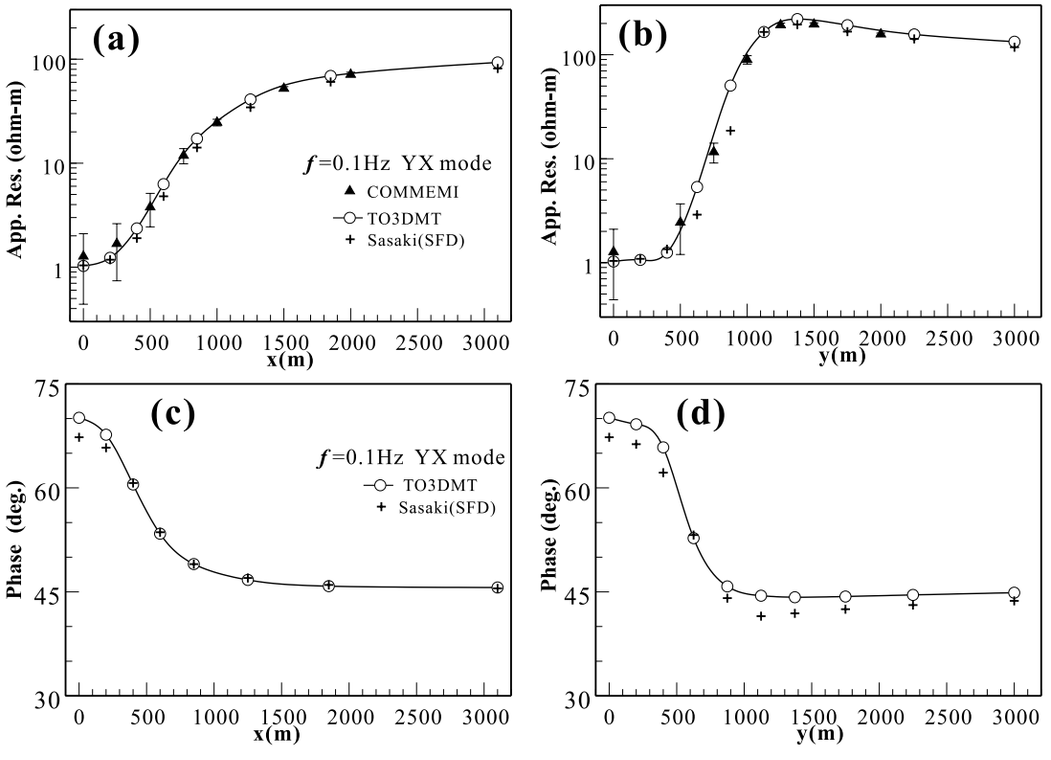

FIG. 6. The *YX*-mode results at 0.1 Hz. See Figure 5 for details.

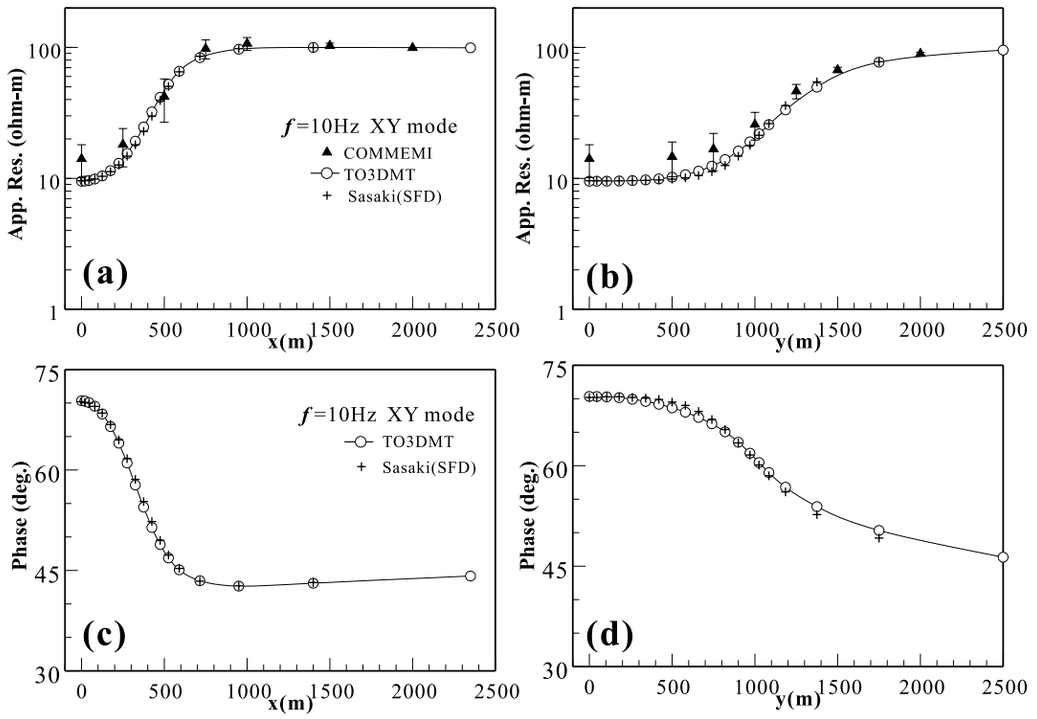

FIG. 8. Comparisons between results obtained using the **T**–Ω finite-element (this study; denoted TO3DMT), staggered-grid FD, and COMMEMI results. The *XY*-mode MT response at 10 Hz is shown in terms of apparent resistivity along the (a) *x*-axis and (b) *y*-axis; phase data are along the (c) *x*-axis and (d) *y*-axis. The mean apparent resistivities of the COMMEMI results are shown with their standard deviations. Information on the mean values of the phase data was not provided in the COMMEMI results.

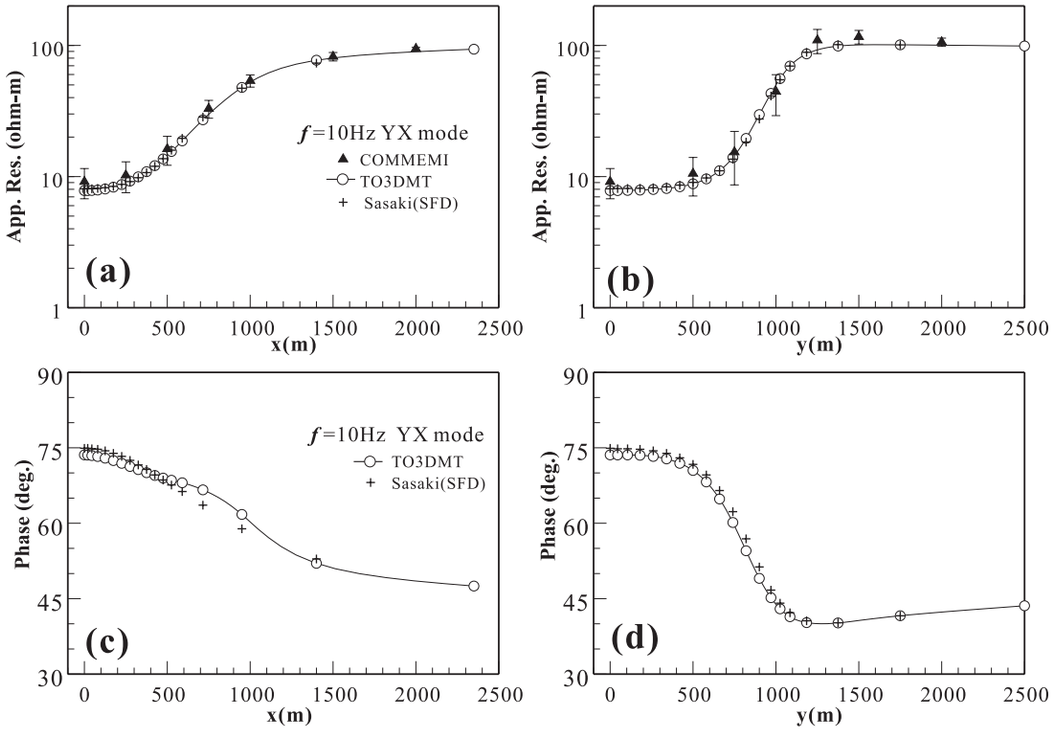

FIG. 9. The *YX*-mode MT response for the COMMEMI 3D-1 model at 10 Hz. See Figure 8 for details.

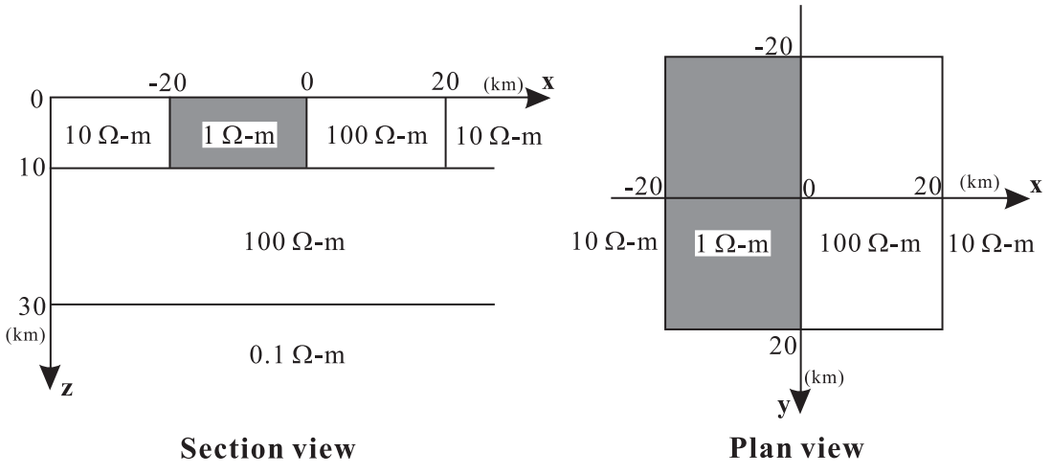

FIG. 10. The COMMEMI 3D-2 model used to compare the finite-element solutions (this study) with the integral-equation solutions. The 3D MT response at 0.001 Hz was computed along the x-axis.

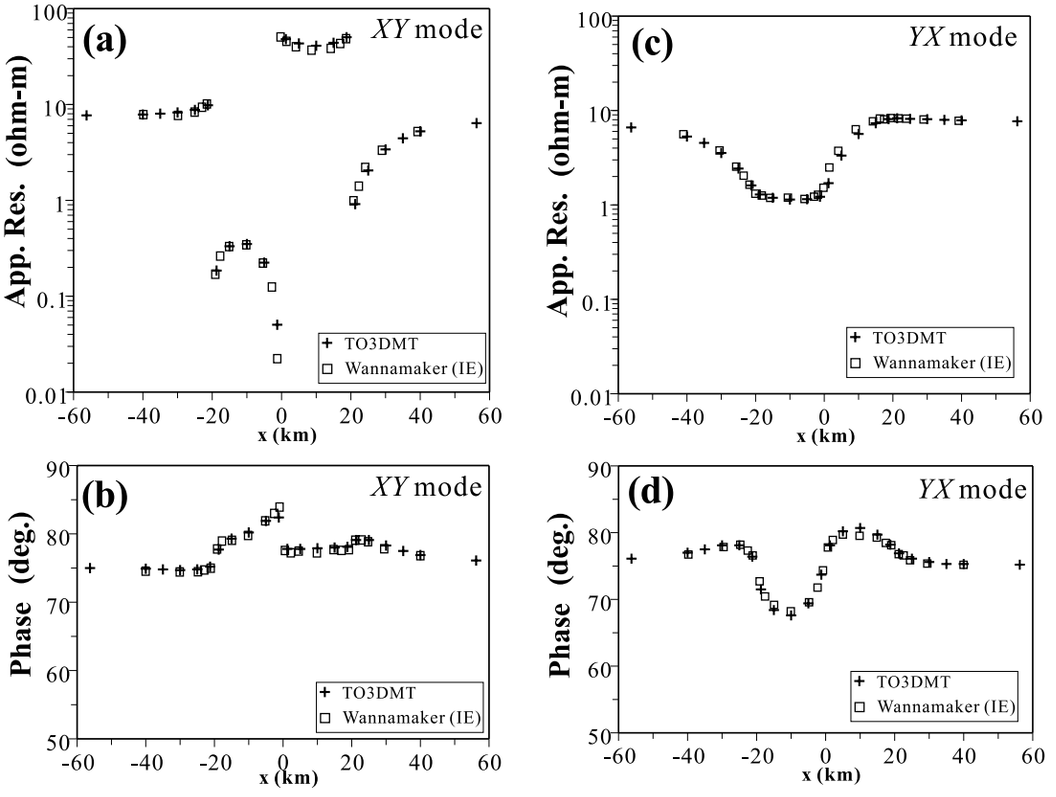

FIG. 11. Comparisons between the finite-element (TO3DMT) and integral-equation solutions for the COMMEMI 3D-2 model at 0.001 Hz: (a) XY-mode apparent resistivity, (b) XY-mode phase data, (c) YX-mode apparent resistivity, and (d) YX-mode phase data.

formulated in terms of **E** or **H**, the system of curl–curl equations for **E** and **H** becomes singular in the air where σ is zero. Thus, it is necessary to approximate the air's conductivity with a small but nonzero value and to use a divergence correction. In our algorithm, however, the curl–curl equation of **T** is only defined in the earth, avoiding instabilities arising from the air's low or zero conductivity. Comparisons with the solutions to two commonly discussed 3D models in the COMMEMI project confirm the validity of our modeling technique. The proposed finite-element modeling method, in addition to integral-equation methods, also represents a useful tool for checking the validity of staggered-grid FD solutions, the accuracy of which has been observed to vary depending on the type of staggered grid used (Siripunvaraporn et al., 2002).

ACKNOWLEDGMENTS

We are grateful to Y. Sasaki for providing the staggered-grid finite-difference results. This work was performed while Y. M. was a visitor at the University of British Columbia on leave from AIST Japan. Y. M. thanks the members of UBC GIF, especially Prof. D. W. Oldenburg for his kind hospitality and Prof. C. G. Farquharson for his encouragement.

REFERENCES

Albanese, R., and Rubinacci, G., 1998, Finite element methods for the solutions of 3D eddy current problems: Advances in Imaging and Electron Physics, **12**, 1–86.

Aruliah, D. A., Ascher, U. M., Haber, E., and Oldenburg, D. W., 2001, A method for the forward modelling of 3D electromagnetic quasi-static problems: Mathematical Models and Methods in Applied Sciences (M3AS), **11**, 1–21.

Avdeev, D. B., Kuvshinov, A. V., Pankratov, O. V., and Newman, G. A., 1997, High performance three dimensional electromagnetic modeling using modified Neumann series: Journal of Geomagnetism and Geoelectricity, **49**, 1519–1539.

Badea, E. A., Everett, M. E., Newman, G. A., and Biro, O., 2001, Finite-element analysis of controlled-source electromagnetic induction using Coulomb-gauged potentials: Geophysics, **66**, 786–799.

Barrett, R., Berry, M., Chan, T. F., Demmeland, J., Donato, J., Dongarra, J., Eijkhout, V., Pozo, R., Romine, C., and Van der Vorst, H., 1994, Templates for the solution of linear systems: Building blocks for iterative methods: Society of Industrial and Applied Mathematics.

Biro, O., and Richter, K. R., 1991, CAD in electromagnetism: Advances in Electronics and Electron Physics, **82**, 1–96.

Carpenter, C. J., 1977, Comparison of alternative formulations of 3-dimensional magnetic field and eddy-current problems at power frequencies: IEE Proceedings, **124**, 1026–1034.

Ellis, R. G., 1999, Joint 3-D electromagnetic inversion, *in* Oristaglio, M., and Spies, B., Eds., Three-dimensional electromagnetics: Society of Exploration Geophysicists, 179–192.

Everett, M. E., and Schultz, A., 1996, Geomagnetic induction in a heterogeneous sphere: Azimuthally symmetric test computations and the response of an undulating 660-km discontinuity: Journal of Geophysical Research, **101**, 2765–2783.

Fomenko, E. Y., and Mogi, T., 2002, A new computation method for a staggered grid of 3D EM field conservative modeling: Earth, Planets, and Space, **54**, 499–509.

Fujiwara, K., Nakata, T., and Ohashi, H., 1996, Improvement of convergence characteristic of ICCG method for the A–ϕ method using edge elements: IEEE Transactions on Magnetics, **32**, 804–807.

Haber, E., Ascher, U. M., Aruliah, D. A., and Oldenburg, D. W., 2000, Fast simulation of 3D electromagnetic problems using potentials: Journal of Computational Physics, **163**, 150–171.

Harrington, R. F., 1961, Time-harmonic electromagnetic fields: McGraw-Hill Book Company.

Jin, J., 1993, The finite element method in electromagnetics: John Wiley & Sons.

Kameari, A., 1988, Three dimensional eddy current calculation using edge elements for magnetic vector potential: First International Symposium, Applied Electromagnetics in Materials, Proceedings, 225–236.

LaBrecque, D. J., 1999, Finite-difference modeling of 3-D EM fields with scalar and vector potentials, *in* Oristaglio, M., and Spies, B., Eds., Three-dimensional electromagnetics: Society of Exploration Geophysicists, 146–160.

Mackie, R. L., Madden, T. R., and Wannamaker, P. E., 1993, Three-dimensional magnetotelluric modeling using difference equations—Theory and comparisons to integral equation solutions: Geophysics, **58**, 215–226.

Mackie, R. L., Smith, J. T., and Madden, T. R., 1994, Three-dimensional electromagnetic modeling using finite difference equations: The magnetotelluric example: Radio Science, **29**, 923–935.

Miya, K., 1995, Analytical electromagnetics and magnetosolid mechanics: Yokendo (in Japanese).

Newman, G. A., and Alumbaugh, D. L., 1995, Frequency-domain modelling of airborne electromagnetic responses using staggered finite differences: Geophysical Prospecting, **43**, 1021–1042.

Saad, Y., 1996, Iterative methods for sparse linear systems: Society of Industrial and Applied Mathematics.

Sasaki, Y., 1999, Three-dimensional frequency-domain electromagnetic modeling using the finite-difference method: Geophys. Explor. (Butsuri Tansa), **52**, 421–431 (in Japanese with English abstract).

——— 2001, Full 3-D inversion of electromagnetic data on PC: Journal of Applied Geophsics, **46**, 45–54.

Silvester, P. P., and Ferrari, R. L., 1996, Finite element methods for electrical engineers: Cambridge University Press.

Siripunvaraporn, W., Egbert, G., and Lenbury, Y., 2002, Numerical accuracy of magnetotelluric modeling: A comparison of finite difference approximations: Earth, Planets, and Space, **54**, 721–725.

Smith, J. T., 1996a, Conservative modeling of 3-D electromagnetic fields, part I: Properties and error analysis: Geophysics, **61**, 1308–1318.

——— 1996b, Conservative modeling of 3-D electromagnetic fields, part II: Biconjugate gradient solution and an accelerator: Geophysics, **61**, 1319–1324.

Steele, C. W., 1997, Numerical computation of electric and magnetic fields: Chapman & Hall.

Ting, S. C., and Hohmann, G. W., 1981, Integral equation modeling of three-dimensional magnetotelluric response: Geophysics, **46**, 182–197.

Tsuboi, H., and Naitoh, T., Eds., 1994, Basics of numerical electromagnetic analysis: Yokendo (in Japanese).

Van der Vorst, H. A., 1992, BI-CGSTAB: A fast and smoothly convergent variant of BI-CG for the solution of nonsymmetric linear systems: SIAM Journal on Scientific and Statistical Computing, **13**, 631–644.

Wannamaker, P. E., 1991, Advances in three-dimensional magnetotelluric modeling using integral equations: Geophysics, **56**, 1716–1728.

Zanoubi, M. R., Jin, J. M., Donepudi, K. C., and Chew, W. C., 1999, A spectral Lanczos decomposition method for solving 3-D low-frequency electromagnetic diffusion by the finite-element method: IEEE Transactions on Antenna Propagation, **47**, 242–248.

Zhdanov, M. S., and Fang, S., 1996, Quasi-linear approximation in 3-D electromagnetic modeling: Geophysics, **61**, 646–665.

Zhdanov, M. S., Varentov, I. M., Weaver, J. T., Golubev, N. G., and Krylov, V. A., 1997, Methods for modelling electromagnetic fields: Results from COMMEMI—The international project on the comparison of modelling methods for electromagnetic induction: Journal of Applied Geophysics, **37**, 133–271.

Zyserman, F. I., and Santos, J. E., 2000, Parallel finite element algorithm with domain decomposition for three-dimensional magnetotelluric modeling: Journal of Applied Geophysics, **44**, 337–351.

APPENDIX A

DIVERGENCE OF THE ELECTRIC VECTOR POTENTIAL AT THE AIR–EARTH INTERFACE

In this appendix, we obtain an expression for the divergence of **T** that includes the Coulomb gauge condition and that can be used throughout the entire problem domain V. As shown in Figure A-1, we consider an earth surface with topography S_c, which is described using a function $g(\,)$ such that $z = g(x, y)$. Simplistically, the Coulomb gauge condition $\nabla \cdot \mathbf{T} = 0$ must be satisfied in V_c [corresponding to $z > g(x, y)$], and $\mathbf{T} = 0$ must be satisfied in V_a [corresponding to $z < g(x, y)$]. However, with respect to the divergence of **T** at the earth's surface S_c, a more careful treatment is needed. We consider an infinitesimal volume ΔV containing an infinitesimal plane ΔS_c that is tangential to S_c and define a local coordinate system of u, v, and w as shown in Figure A-2. The axes of u and v lie within the plane ΔS_c, and the w-axis is the downward normal to ΔS_c. The unit outward normal vector **n** is antiparallel to the w-axis. The divergence of **T** is given by

$$\nabla \cdot \mathbf{T} = \lim_{\Delta u, \Delta v, \Delta w \to 0} \left\{ \frac{T_u(\Delta u) - T_u(-\Delta u)}{2\Delta u} + \frac{T_v(\Delta v) - T_v(-\Delta v)}{2\Delta v} + \frac{T_w(\Delta w) - T_w(-\Delta w)}{2\Delta w} \right\}, \tag{A-1}$$

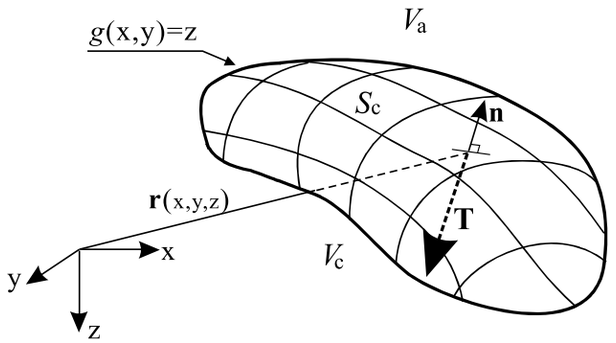

FIG. A-1. A general view of **T** on the earth's surface S_c described by $g(x, y) = z$. The positive direction of **T** is antiparallel to the outward unit normal vector **n**.

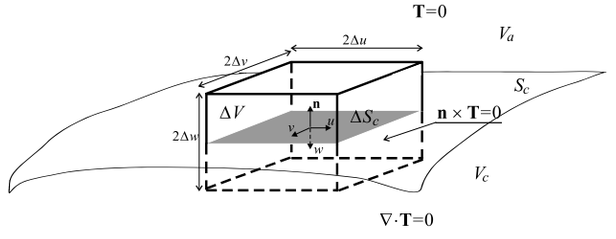

FIG. A-2. An infinitesimal volume ΔV containing a part of S_c. The local coordinate axes u, v, and w are defined in ΔV; and the side lengths of ΔV are denoted by $2\Delta u$, $2\Delta v$, and $2\Delta w$ in the u, v, and w directions, respectively. The infinitesimal tangential plane to S_c is denoted by ΔS_c.

where T_u, T_v, and T_w are components of **T** in the u-, v-, and w-directions, respectively. Considering the condition implied by equation (16) at S_c, we can treat T_u and T_v as zero in ΔV. Consequently, equation (A-1) becomes

$$\nabla \cdot \mathbf{T} = \frac{\partial T_w}{\partial w} \quad \text{in} \quad \Delta V. \tag{A-2}$$

At any point **r** in the lower part of ΔV contained by V_c, or $\mathbf{r} \in \Delta V \cap V_c$, the Coulomb gauge condition $\nabla \cdot \mathbf{T}(\mathbf{r}) = 0$ is satisfied, meaning that $\partial T_w(\mathbf{r})/\partial w = 0$ from equation (A-2). Moreover, T_w is regarded as invariable with respect to u and v within the infinitesimal volume ΔV. Therefore, T_w is a constant value at $\mathbf{r} \in \Delta V \cap V_c$. In addition, because $\mathbf{T} = 0$ in V_a, we can write

$$T_w = T_w^0 U(z - g(x, y)) \quad \text{in} \quad \Delta V, \tag{A-3}$$

where T_w^0 is the value of T_w at S_c and U is the unit step function $U(z \geq g(x, y)) = 1$ and $U(z < g(x, y)) = 0$. The derivative of T_w with respect to w can be written as

$$\frac{\partial T_w}{\partial w} = T_w^0 \frac{\partial U(z - g(x, y))}{\partial w} = T_w^0 \frac{\partial U(f)}{\partial f} \frac{\partial f}{\partial w} \quad \text{in} \quad \Delta V. \tag{A-4}$$

where $f = z - g(x, y)$. Since the gradient of f is parallel to the w-direction, we have $\partial f/\partial w = |\nabla f|$ (see Miya, 1995). Moreover, because $dU(\alpha)/d\alpha = \delta(\alpha)$, the Dirac delta function [equation (A-4)] can be written as

$$\frac{\partial T_w}{\partial w} = T_w^0 \delta(f) |\nabla f| \quad \text{in} \quad \Delta V. \tag{A-5}$$

Given once again that **n** is antiparallel to the w axis and $\delta(f \neq 0) = 0$, and using equations (A-2) and (A-5), we obtain

$$\nabla \cdot \mathbf{T}(\mathbf{r}) = -\mathbf{n} \cdot \mathbf{T}(\mathbf{r}) |\nabla f| \delta(z - g(x, y)), \tag{A-6}$$

where

$$|\nabla f(x, y)| = \sqrt{\left(\frac{\partial g}{\partial x}\right)^2 + \left(\frac{\partial g}{\partial y}\right)^2 + 1}. \tag{A-7}$$

Owing to the characteristics of the delta function, equation (A-6) incorporates the Coulomb gauge condition in V_c and is applicable to the entire problem domain V.

APPENDIX B

DERIVATION OF THE SYSTEM MATRIX FOR THE GALERKIN METHOD

Here we derive the submatrices in the system matrix of the Galerkin finite-element method. Substituting equation (28) into equation (30), we consider the following terms:

$$\begin{aligned}
&\int_{V_c^e} \mathbf{N}_i^e \cdot \nabla \times \left(\frac{1}{\sigma} \nabla \times \mathbf{T}\right) dV \\
&= \int_{V_c^e} \frac{1}{\sigma} (\nabla \times \mathbf{N}_i^e) \cdot (\nabla \times \mathbf{T}) dV \\
&\quad + \int_{V_c^e} \nabla \cdot \left[\left(\frac{1}{\sigma} \nabla \times \mathbf{T}\right) \times \mathbf{N}_i^e\right] dV \\
&= \int_{V_c^e} \frac{1}{\sigma} (\nabla \times \mathbf{N}_i^e) \cdot (\nabla \times \mathbf{T}) dV \\
&\quad + \int_{S^e} \left[\left(\frac{1}{\sigma} \nabla \times \mathbf{T}\right) \times \mathbf{N}_i^e\right] \cdot \mathbf{n} dS \\
&= \int_{V_c^e} \frac{1}{\sigma} (\nabla \times \mathbf{N}_i^e) \cdot (\nabla \times \mathbf{T}) dV \\
&\quad + \int_{S^e} \mathbf{N}_i^e \cdot (\mathbf{n} \times \mathbf{E}) dS,
\end{aligned} \tag{B-1}$$

where the vector formula $\nabla \cdot (\mathbf{A} \times \mathbf{B}) = \mathbf{B} \cdot (\nabla \times \mathbf{A}) - \mathbf{A} \cdot (\nabla \times \mathbf{B})$, Gauss's theorem, and equation (5) are used and where **n** is the outward unit normal vector to the surface S^e of the eth volume element V_c^e. Since the tangential components of **E** are continuous at the interfaces, the second term on the right-hand side of equation (B-1) disappears during the assembly of equation (B-1) for the entire region V_c. Consequently, from equations (28), (30), and (B-1), the submatrices obtained from equation (30) are given by

$$[E^e]_{ij} = \int_{V_c^e} (\nabla \times \mathbf{N}_i^e) \cdot (\nabla \times \mathbf{N}_j^e) dV, \tag{B-2}$$

$$[F^e]_{ij} = \int_{V_c^e} \mathbf{N}_i^e \cdot \mathbf{N}_j^e dV, \tag{B-3}$$

and

$$[H^e]_{ij} = \int_{V_c^e} \mathbf{N}_i^e \cdot \nabla N_j^e dV. \tag{B-4}$$

In addition, using the incident magnetic field $\mathbf{H}_0$, the elements of $\{P^e\}$ are written by

$$\{P^e\}_i = \int_{V_c^e} \mathbf{N}_i^e \cdot \mathbf{H}_0 dV. \tag{B-5}$$

Equation (18) is a type of Poisson equation for the scalar potential. Solving the Poisson equation using the Galerkin finite-element method with nodal elements is a well-known procedure (e.g., see Jin, 1993). The submatrix $[G^e]$ is easily obtained as

$$[G^e]_{ij} = \int_{V^e} \nabla N_i^e \cdot \nabla N_j^e dV. \tag{B-6}$$

In equation (31), the integral of the second term on the right-hand side of equation (29),

$$Q_i^e = -\int_{v^e} N_i^e \mathbf{n} \cdot \mathbf{T}(\mathbf{r}) |\nabla f| \delta(\mathbf{r} \in S_c^e) dV, \tag{B-7}$$

looks complicated; but as it contains the delta function and the gradient of topography, the transformation of this volume integral into a surface integral is relatively straightforward. Only Ω_i^e on S_c^e needs to be taken into account for evaluation (B-7). As shown in Figure B-1, we note the eth volume element V^e containing the surface S_c^e and consider a small volume ΔV^e containing an infinitesimal element of area dS_c^e forming a tangential plane to S_c^e. Within V^e, the local coordinates u, v, and w can be formed such that the u and v axes can lie within S_c^e and w can be the downward normal to S_c^e. As the first step, equation (B-7) is evaluated with respect to ΔV^e. Assuming that $\mathbf{T}(\mathbf{r})$ is constant with respect to u and v within ΔV^e and varies along w, we can write

$$q_i^e = -du\, dv \int_{-d}^{d} N_i^e \mathbf{n} \cdot \mathbf{T}(\mathbf{r}) |\nabla f| \delta(\mathbf{r} \in S_c^e) \det([J]) dw, \tag{B-8}$$

where d is the half-length of ΔV^e along w and $\det([J])$ denotes the determinant of the Jacobian matrix $[J]$, given by

$$[J] = \begin{pmatrix} \dfrac{\partial x}{\partial u} & \dfrac{\partial y}{\partial u} & \dfrac{\partial z}{\partial u} \\ \dfrac{\partial x}{\partial v} & \dfrac{\partial y}{\partial v} & \dfrac{\partial z}{\partial v} \\ \dfrac{\partial x}{\partial w} & \dfrac{\partial y}{\partial w} & \dfrac{\partial z}{\partial w} \end{pmatrix}. \tag{B-9}$$

Since $f = z - g(x, y)$ and $\partial f/\partial u = \partial f/\partial v = 0$, we obtain $|\nabla f| = \partial f/\partial w$. Thus, equation (B-8) can be rewritten as

$$\begin{aligned} q_i^e &= -du\, dv \int_{-d}^{d} N_i^e \mathbf{n} \cdot \mathbf{T}(\mathbf{r}) \det([J]) \delta(\mathbf{r} \in S_c^e) \frac{\partial f}{\partial w} dw \\ &= -du\, dv \int_{-d}^{d} N_i^e \mathbf{n} \cdot \mathbf{T}(\mathbf{r}) \det([J]) \delta(f) df \\ &= -N_i^e \mathbf{n} \cdot \mathbf{T}(\mathbf{r} \in S_c^e) \det([J])_{w=0} du\, dv, \end{aligned} \tag{B-10}$$

where the fact that $f = 0$ and $w = 0$ are satisfied on S_c^e is used. Equation (B-10) shows that the volume integral with respect to ΔV^e equals the surface integral on dS_c^e. Consequently by integrating q_i^e with respect to S_c^e, Q_i^e becomes

$$Q_i^e = \int_{S_c^e} q_i^e = -\int_{S_c^e} N_i^e \mathbf{n} \cdot \mathbf{T} \det([J])_{w=0} du\, dv. \tag{B-11}$$

Since in this paper we deal with a flat earth surface $f = z$, we can write $\mathbf{n} = -\hat{\mathbf{z}}$ and $\det([J]) = 1$. By substituting equation (21) into equation (B-11) for brick elements located immediately below the earth's surface, Q_i^e can be expressed as

$$\begin{pmatrix} Q_0^e \\ \vdots \\ Q_3^e \end{pmatrix} = [Q^e] \begin{pmatrix} T_8^e \\ \vdots \\ T_{11}^e \end{pmatrix}. \tag{B-12}$$

By rewriting equation (B-12) for all N_i^e and $\mathbf{N}_j^e$ in the form of equation (32), the elements of the submatrix $[Q^e]$ in equation (32) are given by

$$\begin{aligned} [Q^e]_{ij} &= \int_{S_c^e} N_i^e |\mathbf{N}_j^e| dS \quad (i = 0 \sim 3 \text{ and } j = 8 \sim 11) \\ &= 0 \qquad\qquad\qquad\quad (\text{otherwise}). \end{aligned} \tag{B-13}$$

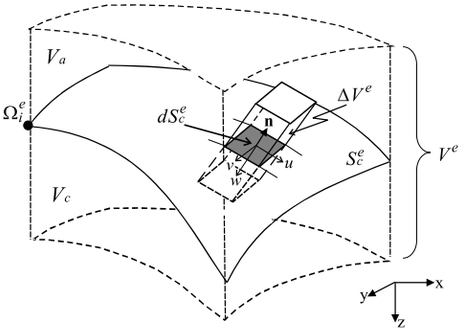

FIG. B-1. The volume integral over the eth volume element V^e containing the air–earth interface S_c^e. The local coordinate axes u, v, and w are defined within V^e such that the u and v axes can lie on S_c^e and the w axis can be normal to S_c^e. To evaluate the integration across S_c^e, a small-volume element ΔV^e containing an infinitesimal plane dS_c^e tangential to S_c^e is considered.